

# Unsupervised LiDAR-Based Multi-UAV Detection and Tracking Under Extreme Sparsity

1<sup>st</sup> Nivand Khosravi   
Instituto Superior Técnico  
University of Lisbon  
Lisbon, Portugal  
nivand.khosravi@tecnico.ulisboa.pt

2<sup>nd</sup> Rodrigo Ventura   
Instituto Superior Técnico  
University of Lisbon  
Lisbon, Portugal  
rodrigo.ventura@tecnico.ulisboa.pt

3<sup>rd</sup> Meysam Basiri   
Instituto Superior Técnico  
University of Lisbon  
Lisbon, Portugal  
meysam.basiri@tecnico.ulisboa.pt

**Abstract**—Non-repetitive solid-state LiDAR scanning leads to an extremely sparse measurement regime for detecting airborne UAVs: a small quadrotor at 10–25 m typically produces only 1–2 returns per scan, which is far below the point densities assumed by most existing detection approaches and inadequate for robust multi-target data association. We introduce an unsupervised, LiDAR-only pipeline that addresses both detection and tracking without the need for labeled training data. The detector integrates range-adaptive DBSCAN clustering with a three-stage temporal consistency check and is benchmarked on real-world air-to-air flight data under eight different parameter configurations. The best setup attains 0.891 precision, 0.804 recall, and 0.63 m RMSE, and a systematic minPts sweep verifies that most scans contain at most 1–2 target points, directly quantifying the sparsity regime. For multi-target tracking, we compare deterministic Hungarian assignment with joint probabilistic data association (JPDA), each coupled with Interacting Multiple Model filtering, in four simulated scenarios with increasing levels of ambiguity. JPDA cuts identity switches by 64% with negligible impact on MOTA, demonstrating that probabilistic association is advantageous when UAV trajectories approach one another closely. A two-environment evaluation strategy, combining real-world detection with RTK-GPS ground truth and simulation-based tracking with identity-annotated ground truth, overcomes the limitations of GNSS-only evaluation at inter-UAV distances below 2 m.

**Index Terms**—UAV detection, LiDAR point cloud, multi-object tracking, data association, JPDA, extreme sparsity

## I. INTRODUCTION

Growing deployment of small UAVs in civilian and security-sensitive airspace demands onboard perception systems that detect aerial targets and maintain consistent track identities. In multi-UAV operations, missed detections and identity switches corrupt relative state estimates, undermining collision avoidance, formation control, and cooperative autonomy [1], [2]. Reliable airborne perception is therefore a foundational requirement for autonomous multi-UAV missions, including leader-follower navigation, coordinated inspection, and swarm operations in GPS-degraded environments.

Among sensing modalities, RF [3] is susceptible to interference; acoustic methods [4] degrade outdoors; vision-based approaches [5] require adequate lighting and appearance cues; and radar exhibits elevated false alarm rates for small, low-RCS targets [6]. LiDAR provides illumination-independent 3D geometry [7] independent of target appearance, making it attractive for onboard aerial perception.

Solid-state LiDAR with non-repetitive scanning creates a perception regime fundamentally different from ground robotics. At 10–25 m, a small quadrotor produces only 1–2 returns per scan due to the rosette pattern that concentrates points non-uniformly each cycle. This extreme sparsity makes fixed-parameter DBSCAN brittle: targets fall below minimum-point thresholds in consecutive scans. In multi-UAV scenarios, overlapping returns from two targets within 1–2 m cannot be reliably disambiguated by deterministic assignment.

Addressing this requires a detector and tracker co-designed for the sparsity regime. The detector must tolerate range-dependent density variation while rejecting background clutter, and the tracker must preserve target identities through trajectory crossings and prolonged detection outages. Per-frame Hungarian matching [8] is efficient but commits irrevocably to a single hypothesis per step, accumulating identity switches under proximity ambiguity. Joint Probabilistic Data Association [9]–[11] distributes likelihood across all feasible hypotheses, offering inherent robustness to measurement ambiguity. IMM filtering [12], [13] handles maneuvering 3D motion via adaptive submodels. Maintaining continuity through LiDAR dropout via adaptive EKF with motion-model switching [14] is a complementary strategy targeting the tracking stage. In contrast, the present work embeds temporal consistency within the detector and provides a controlled comparison of deterministic and probabilistic association for sparse LiDAR multi-UAV tracking. The main contributions of this work are as follows:

- 1) **An unsupervised LiDAR-based detector for extreme sparsity.** We develop a range-adaptive DBSCAN detector with three-stage temporal consistency validation that operates without labeled training data. Evaluated across eight real-world configurations, the best setting achieves 0.891 precision, 0.804 recall, and 0.63 m RMSE. A controlled minPts sweep further shows that most target observations contain only 1–2 points per scan, directly characterizing the underlying sparsity regime.
- 2) **A comparative study of data association for sparse multi-UAV tracking.** We compare deterministic Hungarian assignment and probabilistic JPDA within an IMM-based tracking framework across four simulation

scenarios of increasing association ambiguity. The results show that JPDA reduces identity switches by 64%, from 4.4 to 1.6 on average, at a MOTA cost of only 0.003.

- 3) **A two-environment evaluation protocol for detection and tracking.** We combine real-world air-to-air detection experiments, using RTK-GPS ground truth, with simulation-based tracking experiments that provide unambiguous identity labels at sub-2 m inter-UAV separations. This protocol enables rigorous evaluation in conditions where GNSS-only ground truth is insufficient.

## II. RELATED WORK

### A. LiDAR-Based Aerial Target Detection

Hammer et al. [7] established detection feasibility for sub-0.5 m quadrotors within 30 m using spinning LiDAR, noting rapid point-count decline with range. Razlaw et al. [15] applied temporal integration for cluttered urban environments. Dogru and Marques [16] demonstrated detection with only 3–5 points per target using spatial-temporal features, and Liang et al. [17] achieved unsupervised trajectory estimation without labeled training data.

These works assume spinning LiDAR with repeatable scan patterns and several points per scan. Non-repetitive solid-state sensors such as the Livox Mid-360 use rosette scanning that repositions coverage each cycle, pushing targets to 1–2 points at practical ranges, where fixed clustering fails and cross-frame temporal integration becomes essential.

Learning-based 3D detection architectures including PointNet [18], PointNet++ [19], VoxelNet [20], PointPillars [21], and PointRCNN [22] perform strongly on automotive datasets where targets provide dozens to hundreds of points. These architectures implicitly assume consistent training and test point-density distributions; under extreme sparsity, input distributions shift severely and learned geometric features lose discriminative power. Unsupervised clustering avoids this sensitivity, and range-adaptive DBSCAN [23] naturally compensates for density decay with range without labeled data, a key advantage for resource-constrained deployment.

### B. Data Association for Multi-Target Tracking

AB3DMOT [24], SORT [25], and Deep SORT [26] show Hungarian matching is effective in automotive 3D tracking where detections are dense and targets well-separated. Chiu et al. [27] demonstrated that explicit association uncertainty modeling improves identity consistency in ambiguous scenarios.

Airborne LiDAR tracking differs fundamentally: full-3D maneuvering at higher agility, low detection rates from extreme sparsity, and trajectory crossings as the dominant error source mean standard automotive trackers are unsuitable. We compare Hungarian and JPDA at the tracker level using IMM [12], [13] under controlled scenarios and provide an explicit identity-switch analysis, a comparison not previously reported for this setting.

## III. METHODOLOGY

The system comprises an unsupervised LiDAR detector producing sparse 3D measurements and a multi-object tracker estimating continuous target trajectories using IMM filtering with alternative data-association strategies. Detection operates in the local UAV frame  $\mathcal{F}_L$  for geometric filtering; tracking operates in the global inertial frame  $\mathcal{F}_G$  to keep constant-velocity motion models valid under ego-motion. The modular architecture allows detection configurations and association strategies to be varied independently.

### A. Coordinate Frames and Notation

The local frame  $\mathcal{F}_L$  is body-fixed on the observer UAV; the global frame  $\mathcal{F}_G$  is a world-fixed inertial reference established at initialization. Raw points are processed in  $\mathcal{F}_L$  because geometric constraints (height bounds, radial range limits) are natural in the sensor frame. All tracking operations are performed in  $\mathcal{F}_G$ , ensuring constant-velocity models remain valid under arbitrary ego-rotations and translations.

At discrete time  $t_k$ , the LiDAR scan is an unordered point set  $\mathcal{P}_k = \{\mathbf{p}_k^{(n)} \in \mathbb{R}^3\}_{n=1}^{N_k}$  in  $\mathcal{F}_L$ , where  $N_k$  is the valid return count. The detector outputs  $m_k$  candidate measurements  $\mathcal{Z}_k = \{\mathbf{z}_{k,j}\}_{j=1}^{m_k}$  as cluster centroids in  $\mathcal{F}_L$ , transformed to  $\mathcal{F}_G$  via the known ego-pose before being passed to the tracker.

### B. Unsupervised LiDAR-Based UAV Detection

The detection pipeline extracts validated target measurements through ROI filtering and voxel downsampling, range-adaptive DBSCAN clustering, and three-stage temporal consistency validation, each stage operating under the 1–2 point-per-scan constraint without labeled training data.

1) *Preprocessing and Range-Adaptive Clustering:* Raw clouds  $\mathcal{P}_k$  undergo region-of-interest (ROI) filtering that removes ground returns below height  $h_{\min}$  relative to the sensor, discards far-field points beyond  $r_{\max}$ , and excludes self-returns within a cylindrical exclusion zone of radius  $r_{\text{excl}}$  around the sensor origin to prevent observer-platform interference. Voxel downsampling via the Point Cloud Library [28], [29] is then applied:

$$\mathcal{P}_k^V = \text{VoxelGrid}(\mathcal{P}_k^{\text{ROI}}; v), \quad (1)$$

where voxel size  $v$  controls the spatial resolution–computation trade-off. Each occupied voxel is represented by the centroid of its contained points, retaining geometric fidelity at reduced cardinality [28].

Range-adaptive DBSCAN [23] compensates for inverse-square point-density decay with range. At far distances, the same physical object subtends fewer voxels, so a fixed  $\varepsilon$  would fragment or miss clusters. The neighborhood radius adapts as:

$$\varepsilon(r) = \varepsilon_0 + \alpha \cdot \max(r - r_{\text{ref}}, 0), \quad (2)$$

where  $r = \frac{1}{N_k} \sum_n \|\mathbf{p}_k^{(n)}\|$  is the mean scan range,  $\varepsilon_0$  is the base radius,  $\alpha$  is the range-growth rate (non-zero for adaptive configs C and D; zero otherwise), and  $r_{\text{ref}}$  is the reference distance beyond which expansion activates. Clustering assigns labels via DBSCAN( $\mathcal{P}_k^V; \varepsilon(r), \text{minPts}$ ), where  $\text{minPts}$  is

the minimum point count for a core cluster; noise-labeled points are discarded.

2) *Multi-Layer Validation*: Each candidate cluster  $\mathcal{C} = \{\mathbf{p}_j\}_{j=1}^{n_c}$  passes through three sequential validation layers.

*Layer 1 – Geometric constraints*: Point count and spatial extents must satisfy  $n_{\min} \leq n_c \leq n_{\max}$  and  $\max(e_x, e_y, e_z) < e_{\max}$ , where  $e_d$  denotes the axis-aligned extent along axis  $d$ , bounded by expected UAV dimensions.

*Layer 2 – Spatial jump filtering*: Candidates violating  $\|\mathbf{z}_k - \mathbf{z}_{k-1}\| \leq \max(\tau_{\min}, v_{\max}\Delta t)$  are rejected as physically implausible, where  $\tau_{\min}$  accommodates hovering targets and  $v_{\max}$  bounds maximum velocity.

*Layer 3 – Temporal consistency*: Enabled for single-point configurations, this layer requires at least  $M$  of the last  $K$  candidates to satisfy spatial-temporal proximity:

$$\sum_{i=1}^K \#\{\|\mathbf{z}_k - \mathbf{z}_{k-i}\| < d_{\text{cons}} \wedge t_k - t_{k-i} < T_{\text{cons}}\} \geq M. \quad (3)$$

This layer rejects sporadic noise while preserving spatially consistent sparse returns across time.

Centroid estimation for validated clusters employs component-wise median  $\hat{\mathbf{z}}_k = [\text{med}_j(p_{j,x}), \text{med}_j(p_{j,y}), \text{med}_j(p_{j,z})]^\top$  when  $n_c \geq 3$ , providing robustness against outlier returns from specular reflections or rotor blade hits. For sparser clusters ( $n_c < 3$ ), arithmetic mean is used. The resulting centroid  $\mathbf{z}_{k,j} \in \mathcal{F}_L$  is transformed to  $\mathcal{F}_G$  via the ego-pose and passed to the tracker as a 3D position measurement.

### C. Multi-Object Tracking

1) *State and Measurement Model*: Each track maintains a six-dimensional state  $\mathbf{x}_{k,i} = [\mathbf{p}_{k,i}^\top, \mathbf{v}_{k,i}^\top]^\top \in \mathbb{R}^6$  in  $\mathcal{F}_G$ , evolving under a constant-velocity model:

$$\mathbf{x}_{k|k-1} = \mathbf{F}_k \mathbf{x}_{k-1|k-1} + \mathbf{w}_k, \quad \mathbf{F}_k = \begin{bmatrix} \mathbf{I}_3 & \Delta t_k \mathbf{I}_3 \\ \mathbf{0} & \mathbf{I}_3 \end{bmatrix}. \quad (4)$$

Process noise covariance is  $\mathbf{Q}_k = \mathbf{G}_k q^2 \mathbf{I}_3 \mathbf{G}_k^\top$  with gain  $\mathbf{G}_k = [\frac{1}{2}\Delta t_k^2 \mathbf{I}_3; \Delta t_k \mathbf{I}_3]^\top$ . Detections provide 3D position measurements:

$$\mathbf{z}_{k,j} = \mathbf{H} \mathbf{x}_k + \mathbf{v}_k, \quad \mathbf{H} = [\mathbf{I}_3 \quad \mathbf{0}], \quad \mathbf{v}_k \sim \mathcal{N}(\mathbf{0}, \mathbf{R}). \quad (5)$$

2) *IMM Filtering*: Each track employs an IMM filter [12], [13] with  $M_s = 3$  constant-velocity submodels at noise intensities  $q^{(m)} \in \{q_{\text{low}}, q_{\text{med}}, q_{\text{high}}\}$  capturing hover, cruise, and evasive motion regimes. Model probabilities  $\mu_k^{(m)}$  evolve under Markov transition matrix  $\mathbf{\Pi} = [\pi_{ij}]$ .

*Mixing*: Predicted probabilities  $\mu_{k|k-1}^{(j)} = \sum_i \pi_{ij} \mu_{k-1}^{(i)}$  yield mixing weights  $\mu_{k-1}^{(ij)} = \pi_{ij} \mu_{k-1}^{(i)} / \mu_{k|k-1}^{(j)}$  and mixed initial conditions per model  $j$ :

$$\hat{\mathbf{x}}_{k-1}^{0(j)} = \sum_i \mu_{k-1}^{(ij)} \hat{\mathbf{x}}_{k-1|k-1}^{(i)}, \quad (6)$$

$$\mathbf{P}_{k-1}^{0(j)} = \sum_i \mu_{k-1}^{(ij)} \left[ \mathbf{P}_{k-1|k-1}^{(i)} + \delta^{(ij)} \delta^{(ij)\top} \right], \quad (7)$$

where  $\delta^{(ij)} = \hat{\mathbf{x}}_{k-1|k-1}^{(i)} - \hat{\mathbf{x}}_{k-1}^{0(j)}$ .

*Prediction, update, and fusion*: Each model independently predicts and applies a standard Kalman measurement update. Model probabilities are updated by likelihood weighting:

$$\mu_k^{(j)} = \frac{\Lambda_k^{(j)} \mu_{k|k-1}^{(j)}}{\sum_l \Lambda_k^{(l)} \mu_{k|k-1}^{(l)}}, \quad (8)$$

where  $\Lambda_k^{(j)} = \mathcal{N}(\mathbf{z}_k; \mathbf{H} \hat{\mathbf{x}}_{k|k-1}^{(j)}, \mathbf{S}_k^{(j)})$  is the innovation likelihood. The fused state and covariance are:

$$\hat{\mathbf{x}}_{k|k} = \sum_j \mu_k^{(j)} \hat{\mathbf{x}}_{k|k}^{(j)}, \quad \mathbf{P}_{k|k} = \sum_j \mu_k^{(j)} \left[ \mathbf{P}_{k|k}^{(j)} + \epsilon^{(j)} \epsilon^{(j)\top} \right], \quad (9)$$

where  $\epsilon^{(j)} = \hat{\mathbf{x}}_{k|k}^{(j)} - \hat{\mathbf{x}}_{k|k}$ . Covariance symmetrization and positive-definiteness checks are applied after each step.

3) *Gating and Data Association*: The innovation vector and its covariance are:

$$\mathbf{y}_{k,j} = \mathbf{z}_{k,j} - \mathbf{H} \mathbf{x}_{k|k-1}, \quad \mathbf{S}_k = \mathbf{H} \mathbf{P}_{k|k-1} \mathbf{H}^\top + \mathbf{R}. \quad (10)$$

A detection gates to a track if its squared Mahalanobis distance satisfies  $d^2(\mathbf{z}_{k,j}) = \mathbf{y}_{k,j}^\top \mathbf{S}_k^{-1} \mathbf{y}_{k,j} \leq \gamma$ , where  $\gamma$  is the chi-squared threshold for three degrees of freedom. A wider gate is applied for dormant tracks to facilitate reacquisition after prolonged detection outages. Two association strategies are compared.

*Hungarian assignment* constructs a cost matrix from gated track-detection pairs combining Mahalanobis distance, an identity anchor from the last confident detection, and a velocity-consistency penalty [8]. The optimal one-to-one assignment is computed exactly.

*Joint Probabilistic Data Association* computes marginal association probabilities  $\beta_{i,j}$  and missed-detection probabilities  $\beta_{i,0}$  by enumerating all feasible joint events. The filter update uses the combined innovation  $\mathbf{v}_i = \sum_j \beta_{i,j} (\mathbf{z}_{k,j} - \hat{\mathbf{z}}_{k,i})$  with inflated posterior covariance to account for association uncertainty [9], [10].

4) *Track Management and Evaluation*: Tracks evolve through tentative, confirmed, and dormant states via hit/miss counters. New tracks are initiated from high-confidence unsigned detections subject to a minimum separation constraint to prevent duplicate initialization. Dormant tracks are resurected on detection of a measurement near the last known position, enabling recovery from prolonged detection gaps. Multi-Object Tracking Accuracy is:

$$\text{MOTA} = 1 - \frac{\sum_k (\text{FP}_k + \text{FN}_k + \text{IDSW}_k)}{\sum_k \text{GT}_k}, \quad (11)$$

jointly penalizing false positives, false negatives, and identity switches [30].

## IV. EXPERIMENTAL SETUP

The evaluation employs a two-environment protocol: real-world flights validate detection under genuine sensor sparsity; simulation provides controlled multi-target tracking with unambiguous identity ground truth.

### A. Real-World Detection Experiments

Outdoor flight tests were conducted with two F450 quadrotors at Instituto Superior Técnico, Lisbon. The observer UAV carries an inverted Livox Mid-360 solid-state LiDAR [31] operating at 10 Hz with non-repetitive scanning and nominal 40 m range. Inverted mounting biases the field of view downward and forward for sub-observer target observation. The target is an F450-class quadrotor (450 mm diagonal) executing maneuvers at 5–25 m range. RTK-GPS provides centimeter-level relative ground truth for both platforms (Fig. 1).



Fig. 1. Real-world setup: observer UAV with inverted Livox Mid-360 detecting a target quadrotor at 5–25 m with RTK-GPS ground truth.

The dataset comprises 776 LiDAR scans over approximately 80 s of flight; the target was visible in 628 frames (80.9%) under the region-of-interest protocol. Non-repetitive scanning causes the target to intermittently exit the instantaneous sampling region, and at ranges beyond 10 m a 450 mm quadrotor typically yields only 1–2 returns per scan, making it indistinguishable from background clutter without temporal consistency validation.

Eight detection configurations spanning the precision-recall trade-off are evaluated, varying  $\text{minPts}$ , base radius  $\epsilon_0$ , and voxel size  $v$  (Table I). Configurations C and D activate range-adaptive growth ( $\alpha > 0$ ). All use  $r_{\text{ref}} = 10\text{ m}$ ; Layer 3 is enabled for configs S1, S4, and MR.

### B. Simulation Tracking Experiments

Multi-target tracking requires unambiguous identity ground truth, which GNSS cannot provide reliably within approximately 2 m inter-UAV separation. The MRS UAV System [32] Gazebo simulator provides millimeter-accurate pose estimates with exact identity labels and a LiDAR sensor model reproducing the sparse-return characteristics of actual flight (Fig. 2).

Four scenarios of increasing association difficulty were designed:

- **Sc-I (Occlusion, 968 frames):** Detection gaps of 3–5 s test track maintenance and reacquisition.
- **Sc-II (Crossings, 1708 frames):** Sustained proximity below 3 m with repeated trajectory crossings creates maximum association ambiguity.

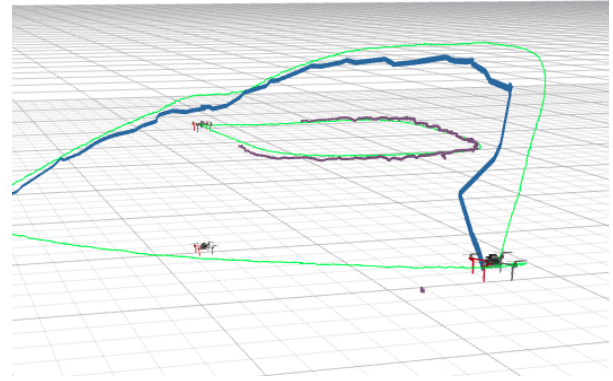


Fig. 2. MRS UAV System Gazebo environment for tracking evaluation with millimeter-accurate ground truth and unambiguous identity labels.

- **Sc-III (Separated, 832 frames):** Inter-target distance consistently above 5 m serves as a low-ambiguity control baseline.
- **Sc-IV (Moderate, 1305 frames):** Intermittent proximity at varying ranges represents mixed operational conditions.

Three simulation detection configurations (Table II) combined with two association methods (Hungarian, JPDA) yield six tracker variants per scenario (24 conditions total).

## V. RESULTS

### A. Real-World Detection Performance

Table I summarizes detection results across eight configurations on 628 visible frames. A fundamental sensor constraint is apparent throughout: the 450 mm target produces only 1–2 returns per scan, limiting achievable detection rate independent of parameter choice.

1) *Sparsity Quantification:* The  $\text{minPts}$  sweep directly quantifies the sparsity regime. Config. S4 ( $\text{minPts} = 4$ ) achieves only 5.6% detection rate, confirming the target rarely provides sufficient point support for strict clustering. Reducing to  $\text{minPts} = 2$  (Config. O) raises the rate to 7.5%, while single-point acceptance with temporal validation (Config. S1,  $\text{minPts} = 1$ ) reaches 39.3%, a sevenfold increase. Config. MR attains 69.9% through balanced temporal validation, representing the practical ceiling under these sensor conditions.

2) *Configuration Analysis:* Config. MR (*Max Recall*) achieves the best overall performance (precision 0.891, recall 0.804, F1 0.845, RMSE 0.63 m). Multi-layer geometric and temporal validation collectively suppresses clutter while retaining spatially consistent sparse returns, yielding a 10.2% false positive rate (36 of 354 detections) at 69.9% detection coverage.

Config. S1 (*Single-Point*) demonstrates that  $\text{minPts} = 1$  is viable under temporal consistency enforcement (Eq. 3), achieving 0.765 precision and 0.77 m RMSE at 39.3% detection rate. Sub-meter accuracy despite single-point acceptance validates the effectiveness of the validation layers.

Config. B (*Failure Mode*) shows the consequence of parameter permissiveness without geometric validation: an RMSE of 2.30 m, which is 3.7 times that of Config. MR, with 45

TABLE I  
REAL-WORLD DETECTION CONFIGURATIONS AND RESULTS (628 VISIBLE FRAMES,  $r_{\text{ref}} = 10 \text{ M}$ ; \*LAYER 3 ENABLED). BEST, VIABLE, FAILURE CONFIGURATIONS.

Configuration Parameters					Detection Results					
Cfg	Name	$\varepsilon_0$ (m)	minPts	$v$ (m)	TP	FP	FN	Prec	Rec	Det%
O	Baseline	0.60	2	0.05	46	1	582	0.979	0.073	7.5
A	Conservative	0.45	3	0.04	21	0	607	1.000	0.033	3.3
B	Permissive	0.70	2	0.06	124	45	504	0.734	0.197	26.9
C	Range-Adaptive	0.60	2	0.04	45	1	583	0.978	0.072	7.3
D	Balanced	0.55	2	0.05	48	1	580	0.980	0.076	7.8
S1	Single-Point*	0.80	1	0.06	189	58	439	0.765	0.301	39.3
S4	Quad-Point*	0.50	4	0.04	28	0	600	1.000	0.045	5.6
MR	Max Recall*	0.80	2	0.07	318	36	310	<b>0.891</b>	<b>0.804</b>	<b>69.9</b>

Note: Det% = percentage of visible frames with a detection. Config B: 2.30m RMSE (failure without geometric validation). minPts reduction from 4 (S4) to 1 (S1) yields a sevenfold detection rate increase (5.6% to 39.3%), confirming extreme per-scan sparsity.

TABLE II  
SIMULATION DETECTION CONFIGURATION PARAMETERS (USED IN TRACKING EVALUATION, SEC. V). VOXEL SIZE IS FIXED BY THE SIMULATION SENSOR MODEL.

Cfg	Name	$\varepsilon_0$ (m)	minPts	Focus
A <sub>s</sub>	Balanced	0.50	3	Precision/recall balance
B <sub>s</sub>	Precision	0.40	2	Low false positives
C <sub>s</sub>	Recall	0.45	3	High measurement coverage

false positives from building edges and pedestrian groups. This establishes that relaxing thresholds alone cannot substitute for principled multi-layer validation.

Conservative configurations (O, A, C, D, S4) achieve RMSE below 0.65 m but detection rates below 8%, suitable only for applications tolerant of highly intermittent measurements.

### B. Multi-Target Tracking Performance

Table III reports tracking results across all four scenarios, three detection configurations, and two association methods. Results are organized by scenario to preserve distinct ambiguity regimes; aggregate rows summarize means across detection configurations.

1) *Per-Scenario Analysis: Sc-I (Occlusion)*. Prolonged detection gaps of 3–5 s expose differences in track reacquisition. Hungarian achieves the highest per-scenario MOTA of 0.628 (Config. A<sub>s</sub>) but accumulates 4–7 identity switches across detection configurations. JPDA eliminates switches entirely under Configs. A<sub>s</sub> and C<sub>s</sub>, demonstrating robustness to sustained detection outages through probabilistic track maintenance.

*Sc-II (Crossings)*. Sustained proximity below 3 m with repeated crossings produces maximum association ambiguity. Hungarian achieves 0.644 MOTA (Config. A<sub>s</sub>) but incurs 10–12 identity switches across all configurations. JPDA reduces switches to 5–7 and yields lower localization error (0.716 m versus 0.760 m under Config. A<sub>s</sub>), consistent with soft-assignment updating mitigating hard-commitment errors during close-range crossing events.

*Sc-III (Separated)*. With inter-target separation consistently above 5 m, both methods yield zero identity switches across all configurations. This confirms that performance differences in Sc-I and Sc-II are attributable to association ambiguity rather than filter instability or motion model mismatch.

*Sc-IV (Moderate)*. Even intermittent proximity benefits probabilistic association. JPDA achieves higher MOTA (0.545 versus 0.508 under Config. A<sub>s</sub>) with zero identity switches, indicating that soft assignment is advantageous beyond exclusively sustained-crossing conditions. Fig. 3 illustrates this scenario: JPDA maintains correct track identities throughout the intermittent proximity events, whereas Hungarian assignment incurs one switch under the same conditions.

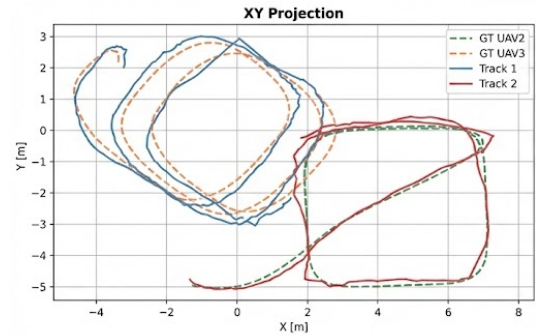


Fig. 3. XY trajectory projection for Sc-IV (Moderate). Ground-truth paths (dashed) and JPDA track estimates (solid) are overlaid for both UAVs. JPDA successfully maintains correct track identities throughout intermittent proximity events, demonstrating its advantage over Hungarian assignment in mixed-ambiguity operational conditions.

2) *Detection Configuration Impact on Tracking*: Config. A<sub>s</sub> (Balanced) yields the highest mean MOTA for Hungarian (0.584 across all scenarios), as balanced precision-recall provides consistent measurement input. Config. C<sub>s</sub> (Recall-biased) benefits JPDA most, enabling 0.570 mean MOTA with zero switches in Sc-I and Sc-IV; increased measurement availability amplifies JPDA’s probabilistic advantage. Config. B<sub>s</sub> (Precision-biased) produces fewest identity switches for both methods but lower mean MOTA (0.551 Hungarian, 0.554 JPDA), as missed detections during critical periods reduce tracking continuity. This detection-association coupling is a key design consideration: recall-biased configurations enhance JPDA through availability, while precision-biased configurations reduce ambiguity at the cost of coverage.

3) *Aggregated Performance*: Aggregating across Sc-I, Sc-II, and Sc-IV (Sc-III excluded as both methods yield zero

TABLE III  
 MULTI-OBJECT TRACKING RESULTS ACROSS SCENARIOS, DETECTION CONFIGURATIONS, AND ASSOCIATION METHODS. JPDA AGGREGATE ,  
 HUNG. AGGREGATE , WORST ID-SWITCH CELLS , BEST PER-SCENARIO MOTA .

		Sc-I: Occlusion (968 fr.)			Sc-II: Crossings (1708 fr.)			Sc-III: Separated (832 fr.)			Sc-IV: Moderate (1305 fr.)		
Det	Assoc	MOTA	RMSE	ID	MOTA	RMSE	ID	MOTA	RMSE	ID	MOTA	RMSE	ID
A	Hung.	0.628	0.624	4	0.644	0.760	10	0.556	0.832	0	0.508	0.500	1
A	JPDA	0.615	0.678	0	0.608	<b>0.716</b>	5	0.556	0.842	0	<b>0.545</b>	0.579	0
B	Hung.	0.626	0.712	7	0.603	0.793	12	0.491	0.585	0	0.506	0.511	1
B	JPDA	0.602	0.711	0	0.601	0.741	7	0.482	0.583	0	0.529	0.487	0
C	Hung.	0.626	0.657	5	0.640	0.778	12	0.536	0.838	0	0.507	0.520	1
C	JPDA	0.612	0.716	0	0.606	0.740	7	<b>0.544</b>	0.841	0	0.544	0.600	0
<i>Aggregate means across detection configurations</i>													
–	Hung.	0.627	0.664	5.3	0.629	0.777	11.3	0.528	0.752	0	0.507	0.510	1.0
–	JPDA	0.610	0.702	0	0.605	<b>0.732</b>	<b>6.3</b>	0.527	0.755	0	<b>0.539</b>	0.555	0

Note: ID = identity switches; RMSE in meters. JPDA reduces switches by 64% (mean 4.4 to 1.6 across Sc-I, Sc-II, Sc-IV) at a MOTA cost of 0.003.

switches) over all detection configurations, JPDA reduces identity switches by 64% (mean 4.4 to 1.6) at a MOTA cost of 0.003 (0.573 to 0.570). Localization error increases marginally by 1.5% (0.676 m to 0.686 m). These results quantify the accuracy-identity trade-off: deterministic assignment favors geometric fidelity through hard measurement commitment, while probabilistic association prioritizes identity preservation under ambiguous interactions at negligible accuracy cost.

## VI. DISCUSSION

### A. Detection Under Extreme Sparsity

The 69.9% detection ceiling despite 80.9% target visibility reflects the intrinsic sensor constraint: at 10–25 m with rosette scanning, a 450 mm quadrotor yields only 1–2 returns per scan, well below the 20+ points assumed by automotive 3D detectors at 70 m [21], [33]. The sevenfold rate increase from Config. S4 to Config. S1 confirms that minPts is the dominant operational parameter and that most scans provide insufficient point support.

Config. MR shows that temporal multi-layer validation enables reliable detection despite per-scan insufficiency; Config. B’s 2.30 m RMSE confirms that permissiveness without geometric validation degrades localization regardless of recall level. Measurement quality must therefore be prioritized over raw detection rate at the detector-tracker interface. This contrasts with [14], which addresses LiDAR dropout via adaptive EKF with motion-model probability switching, without inertial measurements. The two approaches are complementary, targeting different pipeline stages.

### B. Data Association Performance

JPDA’s 64% identity-switch reduction at 0.003 MOTA cost confirms that probabilistic association improves identity preservation under close-proximity ambiguity at negligible accuracy cost. Gains are scenario-dependent: both methods perform equivalently under separation (Sc-III), while JPDA

advantages emerge clearly during crossings (Sc-II) and intermittent proximity (Sc-IV). Hungarian achieves marginally higher instantaneous MOTA through aggressive geometric fitting, but hard commitment during ambiguous interactions accumulates identity errors costly for cooperative localization and collision avoidance. JPDA’s modest RMSE increase (0.676 m to 0.686 m) is a favorable exchange when long-term track continuity is required.

### C. System Implications and Limitations

Config. MR or Config. S1 is recommended for state estimation; Hungarian is appropriate for well-separated targets; JPDA is preferred whenever identity continuity matters during close maneuvers. Temporal consistency validation is essential; threshold tuning alone is insufficient, as Config. B confirms.

Limitations include single-target real-world validation; reliable multi-UAV ground truth at close range requires UWB-based localization [34] or motion capture. JPDA scales combinatorially and requires JIPDA [35] for swarms. IMM parameters require recalibration for different platform dynamics.

## VII. CONCLUSION

Solid-state LiDAR imposes a hard sparsity floor in airborne UAV perception: at 10–25 m, a 450 mm quadrotor yields only 1–2 returns per scan due to non-repetitive rosette scanning, irrespective of parameter choice. This work showed that reliable operation within this regime requires co-design of detector and tracker rather than threshold tuning alone.

On detection, three-stage temporal consistency validation achieves 0.891 precision and 0.804 recall with 0.63 m RMSE, approaching the physical 69.9% detection ceiling. Permissive clustering without geometric validation degrades localization to 2.30 m RMSE, confirming that measurement quality dominates over raw detection rate at the detector-tracker interface.

On tracking, JPDA reduces identity switches by 64% over Hungarian at 0.003 MOTA cost. Gains concentrate in crossing and intermittent-proximity scenarios and are amplified by recall-biased detection, establishing a detector-tracker

coupling: high-recall detection feeds more measurements to JPDA, directly amplifying its probabilistic advantage.

The two-environment protocol, combining real-world RTK-GPS detection validation with simulation-based identity-labeled tracking, provides a sound methodology for systems where GNSS ground truth is insufficient at close inter-UAV separations. Future work will extend to per-layer ablation studies, real-world multi-UAV tracking with UWB-based relative localization, and swarm-scale JPDA approximations.

#### ACKNOWLEDGMENT

The authors acknowledge the financial support provided by the Aero.Next Project under Grant Nos. C645727867 and 00000066.

#### REFERENCES

- [1] M. Ritchie, F. Fioranelli, H. Griffiths, and B. Torvik, "Micro-drone RCS analysis," in *Proc. IEEE Radar Conf. (RadarConf)*, 2015, pp. 452–456.
- [2] P. Nguyen, M. Ravindranatha, A. Nguyen, R. Han, and T. Vu, "Investigating cost-effective RF-based detection of drones," in *Proc. ACM DroNet Workshop*, 2016, pp. 17–22.
- [3] M. Ezuma, F. Erden, C. K. Anjinappa, O. Ozdemir, and I. Guvenc, "Detection and classification of UAVs using RF fingerprints in the presence of Wi-Fi and Bluetooth interference," *IEEE Open Journal of the Communications Society*, vol. 1, pp. 60–76, 2020.
- [4] M. Basiri, F. Schill, P. Lima, and D. Floreano, "On-board relative bearing estimation for teams of drones using sound," *IEEE Robotics and Automation Letters*, vol. 1, no. 2, pp. 820–827, Jul. 2016.
- [5] A. Rozantsev, V. Lepetit, and P. Fua, "Detecting flying objects using a single moving camera," *IEEE Trans. Pattern Anal. Mach. Intell.*, vol. 39, no. 5, pp. 879–892, 2017.
- [6] S. Björklund and A. Öhman, "Target detection and classification of small drones by deep learning on radar micro-Doppler," in *Proc. European Radar Conf. (EuRAD)*, 2018, pp. 182–185.
- [7] M. Hammer, M. Hebel, M. Laurenzis, and M. Arens, "LiDAR-based detection and tracking of small UAVs," in *Proc. SPIE*, vol. 10799, 2018, paper 107990S.
- [8] H. W. Kuhn, "The Hungarian method for the assignment problem," *Naval Research Logistics Quarterly*, vol. 2, no. 1-2, pp. 83–97, 1955.
- [9] Y. Bar-Shalom and T. E. Fortmann, *Tracking and Data Association*. San Diego, CA, USA: Academic Press, 1988.
- [10] T. Fortmann, Y. Bar-Shalom, and M. Scheffe, "Sonar tracking of multiple targets using joint probabilistic data association," *IEEE Journal of Oceanic Engineering*, vol. 8, no. 3, pp. 173–184, Jul. 1983.
- [11] S. H. Rezatofighi, A. Milan, Z. Zhang, Q. Shi, A. Dick, and I. Reid, "Joint probabilistic data association revisited," in *Proc. IEEE Int. Conf. Comput. Vis. (ICCV)*, 2015, pp. 3047–3055.
- [12] H. A. P. Blom and Y. Bar-Shalom, "The interacting multiple model algorithm for systems with Markovian switching coefficients," *IEEE Trans. Autom. Control*, vol. 33, no. 8, pp. 780–783, Aug. 1988.
- [13] X. R. Li and V. P. Jilkov, "Survey of maneuvering target tracking. Part I: Dynamic models," *IEEE Trans. Aerosp. Electron. Syst.*, vol. 39, no. 4, pp. 1333–1364, Oct. 2003.
- [14] N. Khosravi, M. Basiri, and R. Ventura, "Lightweight 3D LiDAR-based UAV tracking: An adaptive extended Kalman filtering approach," 2026. [Online]. Available: <https://arxiv.org/abs/2603.09783>
- [15] J. Razlaw, D. Quiskamp, D. Burschka, and M. Lauer, "Detection and tracking of small UAVs in dense urban environments," in *Proc. IEEE Int. Conf. Robot. Autom. (ICRA)*, 2019, pp. 1266–1272.
- [16] S. Dogru and L. Marques, "Drone detection using sparse LiDAR measurements," *IEEE Robotics and Automation Letters*, vol. 7, no. 2, pp. 3062–3069, Apr. 2022.
- [17] H. Liang, S. Cao, Z. Wang, and J. Liu, "Unsupervised UAV 3D trajectories estimation with sparse point clouds," arXiv preprint, 2024.
- [18] C. R. Qi, H. Su, K. Mo, and L. J. Guibas, "PointNet: Deep learning on point sets for 3D classification and segmentation," in *Proc. IEEE Conf. Comput. Vis. Pattern Recognit. (CVPR)*, 2017, pp. 652–660.
- [19] C. R. Qi, L. Yi, H. Su, and L. J. Guibas, "PointNet++: Deep hierarchical feature learning on point sets in a metric space," in *Advances in Neural Information Processing Systems (NeurIPS)*, vol. 30, 2017.
- [20] Y. Zhou and O. Tuzel, "VoxelNet: End-to-end learning for point cloud based 3D object detection," in *Proc. IEEE Conf. Comput. Vis. Pattern Recognit. (CVPR)*, 2018, pp. 4490–4499.
- [21] A. H. Lang, S. Vora, H. Caesar, L. Zhou, J. Yang, and O. Beijbom, "PointPillars: Fast encoders for object detection from point clouds," in *Proc. IEEE/CVF Conf. Comput. Vis. Pattern Recognit. (CVPR)*. IEEE, 2019, pp. 12 697–12 705.
- [22] S. Shi, X. Wang, and H. Li, "PointRCNN: 3D object proposal generation and detection from point cloud," in *Proc. IEEE/CVF Conf. Comput. Vis. Pattern Recognit. (CVPR)*. IEEE, 2019, pp. 770–779.
- [23] M. Ester, H.-P. Kriegel, J. Sander, and X. Xu, "A density-based algorithm for discovering clusters in large spatial databases with noise," in *Proc. Int. Conf. Knowledge Discovery and Data Mining (KDD)*, 1996, pp. 226–231.
- [24] X. Weng, J. Wang, D. Held, and K. Kitani, "AB3DMOT: A baseline for 3D multi-object tracking and new evaluation metrics," in *Proc. IEEE/RSJ Int. Conf. Intelligent Robots and Systems (IROS)*, 2020, pp. 10 359–10 366.
- [25] A. Bewley, Z. Ge, L. Ott, F. Ramos, and B. Upcroft, "Simple online and realtime tracking," in *Proc. IEEE Int. Conf. Image Process. (ICIP)*, 2016, pp. 3464–3468.
- [26] N. Wojke, A. Bewley, and D. Paulus, "Simple online and realtime tracking with a deep association metric," in *Proc. IEEE Int. Conf. Image Process. (ICIP)*, 2017, pp. 3645–3649.
- [27] H.-K. Chiu, A. Prioletti, J. Li, and J. Bohg, "Probabilistic 3D multi-modal, multi-object tracking for autonomous driving," in *Proc. IEEE Int. Conf. Robot. Autom. (ICRA)*, 2021, pp. 14 227–14 233.
- [28] R. B. Rusu and S. Cousins, "3D is here: Point Cloud Library (PCL)," in *Proc. IEEE Int. Conf. Robot. Autom. (ICRA)*. IEEE, 2011, pp. 1–4.
- [29] D. Holz, A. E. Ichim, F. Tombari, R. B. Rusu, and S. Behnke, "Registration with the point cloud library: A modular framework for aligning in 3-d," *IEEE Robotics & Automation Magazine*, vol. 22, no. 4, pp. 110–124, 2015.
- [30] K. Bernardin and R. Stiefelhagen, "Evaluating multiple object tracking performance: The CLEAR MOT metrics," *EURASIP Journal on Image and Video Processing*, vol. 2008, pp. 1–10, 2008.
- [31] Z. Liu, F. Zhang, and X. Hong, "Low-cost retina-like robotic LiDAR for 3D dense depth sensing," *Sensors*, vol. 20, no. 9, p. 2582, 2020.
- [32] T. Baca, M. Petrik, M. Vrba, V. Spurny, R. Penicka, D. Hert, and M. Saska, "The MRS UAV system: Pushing the frontiers of reproducible research, real-world deployment, and education with autonomous unmanned aerial vehicles," *Journal of Intelligent & Robotic Systems*, vol. 102, no. 26, pp. 1–28, 2021.
- [33] C. R. Qi, W. Liu, C. Wu, H. Su, and L. J. Guibas, "Frustrum PointNets for 3D object detection from RGB-D data," in *Proc. IEEE Conf. Comput. Vis. Pattern Recognit. (CVPR)*. IEEE, 2018, pp. 918–927.
- [34] M. W. Mueller, M. Hamer, and R. D'Andrea, "Fusing ultra-wideband range measurements with accelerometers and rate gyroscopes for quadcopter state estimation," in *Proc. IEEE Int. Conf. Robot. Autom. (ICRA)*, 2015, pp. 1730–1736.
- [35] D. Musicki, R. Evans, and S. Stanković, "Integrated probabilistic data association," *IEEE Trans. Autom. Control*, vol. 39, no. 6, pp. 1237–1241, Jun. 1994.